J Adv Ceram

Research Article

# Oxygen vacancy-rich engineering-optimized molybdenum trioxide microbelts for room-temperature ppb-level trimethylamine detection

Kaidi Wu[1,2], Zhijie Xu[1,2], Kaichun Xu[1,2,3], Jinyong Xu[1,2], Yifan Luo[1,2], Marc Debliquy[4], Chao Zhang[1,2,✉]

Cite this article: Wu K, Xu Z, Xu K, et al. *J Adv Ceram* 2025, **14**(7): 9221102. https://doi.org/10.26599/JAC.2025.9221102

**ABSTRACT:** Oxygen vacancies in metal oxides play a pivotal role in determining their electronic structure and interfacial redox dynamics. However, their sluggish kinetics and imbalanced adsorption/desorption hinder their performance. Here, we report oxygen vacancy ($O_V$)-rich molybdenum trioxide ($MoO_3$) microbelts for room-temperature (RT) volatile organic compound (VOC) sensors, effectively overcoming these limitations. Owing to the synergistic effects of a large specific surface area, surface oxygen vacancies, and an optimized electronic structure, exceptional trimethylamine (TMA) sensing performance richs oxygen vacancy-$MoO_3$ ($MoO_{3-x}$-R), including notably high response, rapid response/recovery, high selectivity, a low limit of detection (400 ppb), and reliable operational stability, was achieved. Experimental and density functional theory studies revealed that controlled oxygen vacancies contribute to tuning the surface redox activity of one-dimensional (1D) $MoO_3$ and regulating the interfacial electron transfer efficiency. Molecular dynamics (MD) simulations revealed that abundant oxygen vacancies in $MoO_{3-x}$-R enhance its affinity for TMA while weakening its interaction with nitrogen, carbon dioxide, or water vapor. Furthermore, a portable device was developed for quantitative TMA monitoring, enabling rapid and nondestructive detection of fish freshness. This research provides novel perspectives for designing high-performance gas sensors by optimizing the interfacial redox kinetics.

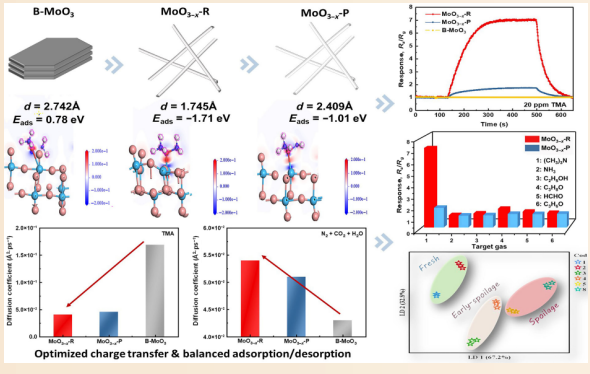


**KEYWORDS:** oxygen vacancy ($O_V$)-rich engineering; molybdenum trioxide ($MoO_3$); gas sensor; room temperature; volatile organic compound (VOC) detection

## 1 Introduction

The effective detection of harmful gases via cost-effective gas sensors plays a key role in public health, environmental protection, and industrial safety. Among them, metal oxide-based (MOX) chemiresistive gas sensors are gaining importance in environmental monitoring, food safety detection, and healthcare diagnosis because of their easy integration and cost effectiveness [1]. Nevertheless, MOXs commonly need to operate at high temperatures (100–500 °C) to overcome the energy barriers of redox reactions, resulting in high power consumption, poor safety, and operational stability [2,3]. In addition, a high working temperature requires a heater unit, leading to increased costs and complexity in the fabrication process [4]. Consequently, gas sensors that function at room temperature (RT) have garnered significant attention. Designing unique morphologies, decorating catalysts (metal elements, metal oxides, etc.), constructing heterostructures, and coupling carbon-based nanomaterials have also been reported to realize the RT response of MOXs to $H_2S$, $NO_2$, and $NH_3$ [5–7]. Among these materials, molybdenum trioxide ($MoO_3$) has a unique layered structure, tunable band gap (2.7–3.5 eV), high electron mobility, nontoxicity, and good electrochemical properties, and has been widely explored as an effective gas sensor [8]. However, achieving rapid detection of volatile organic compounds (VOCs) with high sensitivity and selectivity at RT using $MoO_3$ without catalysts and revealing the gas-sensing mechanism remains challenging.

Oxygen vacancy ($O_V$) engineering has been employed to improve the surface activity and electronic structure of MOXs, thereby increasing their performance in heterocatalysis, energy storage, and gas sensing applications [9,10]. Notably, the presence of oxygen vacancies can supply free electrons and serve as active

[1]College of Mechanical Engineering, Yangzhou University, Yangzhou 225127, China. [2]Jiangsu Key Laboratory of Surface Strengthening and Functional Manufacturing (Yangzhou University), Yangzhou 225127, China. [3]ICB UMR 6303, CNRS, Univ. Bourgogne Franche-Comté, UTBM, Belfort 90010, France. [4]Service de Science des Matériaux, Faculté Polytechnique, Université de Mons, Mons 7000, Belgium.

✉ Corresponding author. E-mail: zhangc@yzu.edu.cn

Received: March 24, 2025; Revised: May 12, 2025; Accepted: May 27, 2025

sites for the adsorption of molecules, thus influencing the capacity to capture electrons and reduce reaction barriers, all of which are paramount in enhancing the efficacy of sensing materials [11]. For example, Zhou *et al.* [12] reported that Na–ZnO exhibited a significantly high response to formaldehyde (21.3@5 ppm) and a low limit of detection (298 ppb), which was attributed to the high content of oxygen vacancies (20.98%), modulated band structure, and active electron transitions. Zeb *et al.* [13] reported that a bimetal (Ni and Co) codoped $W_{18}O_{49}$ crystal lattice leads to the generation of oxygen vacancies and electronic structure modulation, which improve the redox capability and catalytic efficiency of the $W_{18}O_{49}$ sensor to triethylamine. Hence, regulating the electronic properties and surface activity of MOXs is crucial for realizing RT-sensing functions. Specifically, controlling the oxygen vacancies of metal oxides is a promising approach for developing high-performance RT gas sensors, but it is also urgent to offer mechanistic insight into the improved limit of detection (LOD) and response and recovery speed enabled by oxygen vacancies.

In this case, trimethylamine (TMA), which is a harmful gas with a characteristic fishy odor recognized for adverse effects on human health and the environment, was selected as the target biomarker gas [14,15]. Notably, remaining in an environment with a TMA concentration below 10 ppm for over 10 min would result in severe harm [16]. Usually, stale seafood and meat also release a certain concentration of TMA, and the concentration of volatile TMA (10 ppm) is recommended as a criterion to assess spoilage [17,18]. Additionally, patients with renal impairment and trimethylaminuria are unable to metabolize trimethylamine effectively, which will cause a variation in TMA concentration and release a fishy odor through respiration [19,20]. Therefore, TMA can also be a biomarker for the noninvasive diagnosis of kidney disease and trimethylaminuria. Hence, developing reliable and rapid TMA detection techniques is necessary for health assessment and environmental protection.

In this study, we developed controlled oxygen vacancy-mediated $MoO_3$ ($MoO_{3-x}$-R) microbelts via simple hydrothermal synthesis and calcination routes. The prepared $MoO_{3-x}$-R showed a high response to TMA ($R_a/R_g$ = 7.1@20 ppm, where $R_a$ and $R_g$ represent the stable resistance values in air and the target gas), fast response/recovery speed, and a low limit of detection (400 ppb). From the density functional theory (DFT) and molecular dynamics (MD) results, the effective detection of TMA is ascribed to the dynamic modulation of the oxygen vacancies, electronic structure, and interfacial charge dynamics, which strongly activate the gas molecules and the adsorption/desorption balance on the surface of $MoO_{3-x}$-R and electron transfer. The as-fabricated gas sensor and portable device were also demonstrated for quantitative TMA monitoring and real-time fish freshness detection. This work offers insight into unraveling improved sensing mechanisms and designing cost-effective and practical gas sensors.

## 2 Experimental

### 2.1 Synthesis of $MoO_{3-x}$-R and $MoO_{3-x}$-P microbelts

Bulk $MoO_3$ (B-$MoO_3$) was first prepared as follows: 10 g ammonium molybdate tetrahydrate was calcined at 500 °C for 2 h at a heating rate of 5 °C·min$^{-1}$. Then, 0.72 g of B-$MoO_3$ was dispersed in a mixed solution of nitric acid (65 wt%, 2.6 mL) and hydrogen peroxide (5.4 mL). After magnetic stirring for 20 min, the resulting suspension was transferred into a Teflon-stainless steel autoclave (100 mL), which was heated at 170 °C for 24 h. The final product was washed 4 times with deionized water and anhydrous ethanol and subsequently dried at 70 °C for 12 h. This sample was denoted as $MoO_{3-x}$-R. The sample was then calcined at 400 °C for 2 h and denoted as $MoO_{3-x}$-P.

### 2.2 Characterizations

The phase structure was investigated via an X-ray diffractometer (XRD; D8 Advance, Bruker, USA) using Cu-Kα radiation ($\lambda$ = 1.5418 Å). The morphological and nanostructure details were observed via a field-emission scanning electron microscope (FESEM; S4800II, Hitachi, Japan), a transmission electron microscope (TEM; JEM-2100, JEOL, Japan), and a high-resolution transmission electron microscope (HRTEM; Tecnai G2 F30 S-TWIN, FEI, USA). The chemical states of the elements and valence band (VB) spectra were obtained via an X-ray photoelectron spectrometer (XPS; ESCALAB MK II, VG Scientific, UK) with a Mg X-ray source. Nitrogen ($N_2$) sorption isotherms were measured via the Autosorb IQ3 (Quantachrome Instruments, USA). The ultraviolet–visible (UV–Vis) diffuse reflectance spectra were recorded on a UV–Vis spectrophotometer (UV-3600, Shimadu, Japan) with an integrating sphere and $BaSO_4$ as a reference. Fourier transform infrared (FT-IR) spectra were obtained via a spectrometer (IFS 66 v/s FTIR, Bruker, USA). The presence of oxygen vacancies was confirmed by a photoluminescence (PL) spectroscope (325 nm He-Cd Lasers, Thermo Fisher, USA).

### 2.3 Fabrication and measurement of gas sensors

The pastes were prepared by mixing the powders with deionized water and then coated onto the $Al_2O_3$ substrates, which were kept at 125 °C for 24 h. The room temperature (22±3 °C) gas sensor testing system is displayed in Fig. S1 in the Electronic Supplementary Material (ESM). More testing information can also be found in the ESM. The n-type response of a fabricated gas sensor is defined as $R_a/R_g$. The response/recovery time is taken from the time when the total resistance change reaches 90%.

### 2.4 Computational details

The DFT calculation was carried out via the Cambridge Sequential Total Energy Package (CASTEP) modules. The adsorption energy ($E_{ads}$) of TMA molecules on $MoO_{3-x}$ was calculated as follows: $E_{ads} = E_{total} - (E_{surface} + E_{gas})$, where $E_{total}$ is the system's total energy after adsorbing the gas, $E_{surface}$ is the energy of the material surface when the gas is not adsorbed, and $E_{gas}$ is the energy of the isolated gas molecule. Other setting details can be found in the ESM.

All the molecular dynamics (MD) simulations were performed via the Forcite modules. The temperature of each confined case was maintained at 296 K. The systems were first equilibrated for 10 ps to obtain a stable system. After that, we added 5 molecules of nitrogen, 10 molecules of carbon dioxide, and 10 molecules of water to each system. Another 10 ps of the simulation was performed for whole-case relaxation. More setting details are provided in the ESM.

## 3 Results and discussion

### 3.1 Characterizations

Figure 1(a) illustrates the preparation procedures for bulk $MoO_3$ and rich-oxygen-vacancy-mediated $MoO_3$ microbelts. The $MoO_{3-x}$-R microbelts were successfully prepared via a hydrothermal synthesis method in a strongly oxidized solvent. To further clarify the effect of the oxygen vacancy concentration, $MoO_{3-x}$ microbelts with lower concentrations of oxygen vacancies ($MoO_{3-x}$-P) were prepared via calcination in air. As depicted in

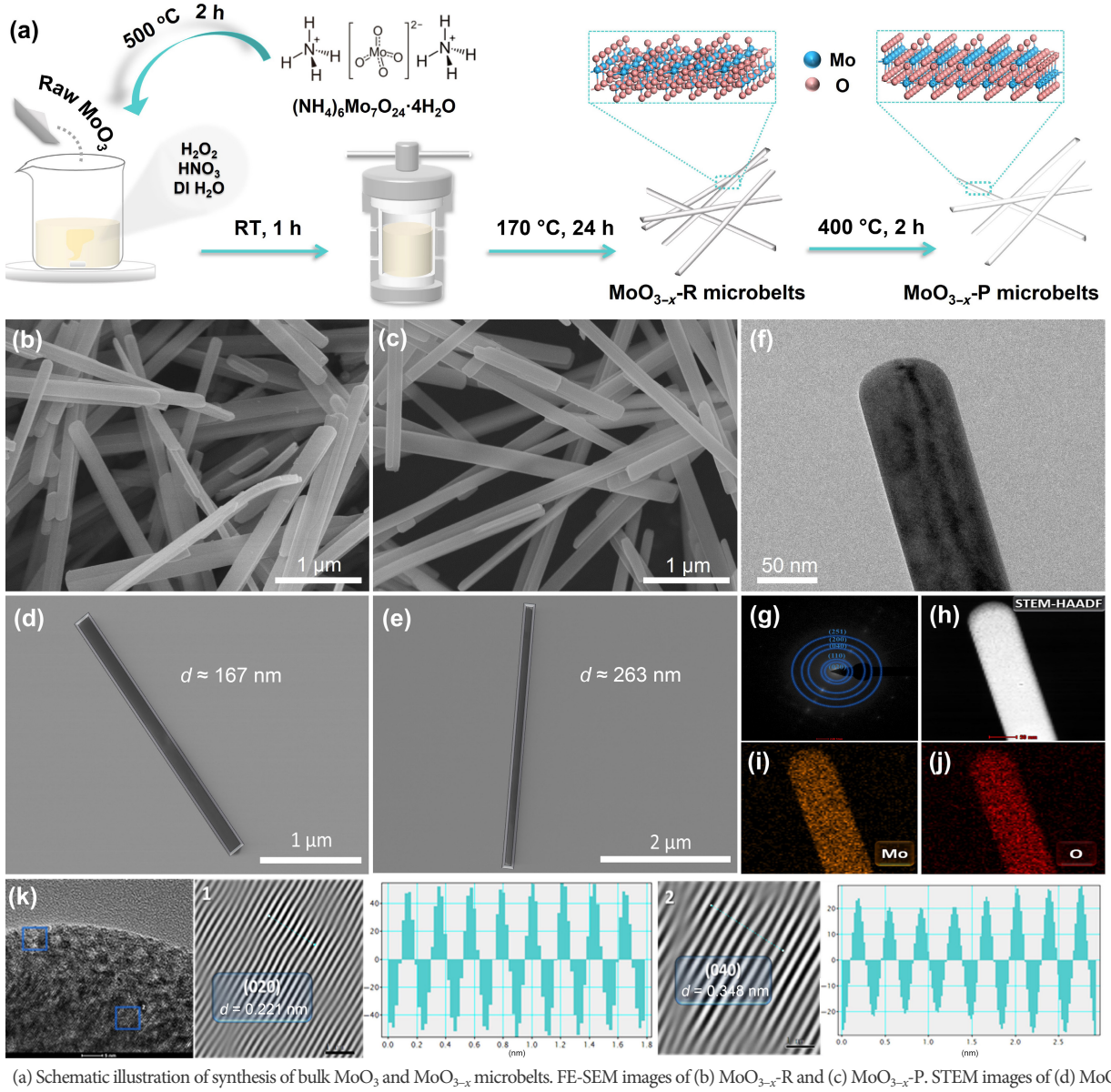


**Fig. 1** (a) Schematic illustration of synthesis of bulk $MoO_3$ and $MoO_{3-x}$ microbelts. FE-SEM images of (b) $MoO_{3-x}$-R and (c) $MoO_{3-x}$-P. STEM images of (d) $MoO_{3-x}$-R and (e) $MoO_{3-x}$-P. Characterization of $MoO_{3-x}$-R microbelts: (f) HRTEM images, (g) SAED pattern, (h) HAADF-STEM image, (i, j) EDS mappings, and (k) lattice information.

Fig. S2 in the ESM, the as-prepared bulk $MoO_3$ has a thick sheet structure of varying sizes, whereas the as-synthesized $MoO_{3-x}$-R and $MoO_{3-x}$-P have one-dimensional (1D) microbelts with a uniform diameter (Figs. 1(b) and 1(c) and Fig. S3 in the ESM). The diameter of $MoO_{3-x}$-R is approximately 167 nm, and that of $MoO_{3-x}$-P is ~263 nm, which is attributed to the second growth during the calcination process. The HRTEM images and selected area electron diffraction (SAED) patterns confirmed the 1D morphology and crystal phase structure of both samples (Figs. 1(f) and 1(g) and Figs. S4(a) and S4(b) in the ESM). The energy dispersive spectroscopy (EDS) mappings show that the main elements of both samples are Mo and O, which are evenly distributed throughout the whole microbelt (Figs. 1(h) and 1(j) and Fig. S4(c) in the ESM). Figure 1(k) shows lattice fringes with interplanar spacings of 0.221 and 0.348 nm, corresponding to the (020) and (040) crystal planes of $MoO_{3-x}$-R. $MoO_{3-x}$-P has slightly larger interplanar spacings of approximately 0.224 and 0.351 nm (Fig. S5 in the ESM).

Powder X-ray diffraction (PXRD) was used to analyze the crystal phase structure of the as-synthesized samples. As shown in Fig. 2(a), the characteristic peaks observed at 10°–80° match the standard pattern of orthorhombic $MoO_3$ (JCPDS No. 05-0508). In particular, the three strong peaks are indexed to the (020), (040), and (060) crystallographic planes of orthorhombic-phase $MoO_3$. Conversely, the remaining peaks exhibit significantly lower intensities, suggesting favorable growth along the [010] direction, which is confirmed through HRTEM images [21]. Interestingly, the characteristic peak of $MoO_3$ remains unchanged after altering the oxygen vacancy concentration, indicating that the manipulation of the oxygen vacancy does not influence the crystal structure. As shown in Fig. 2(b), three peaks at 809.6, 861.5, and 975.6 $cm^{-1}$ are attributed to the stretching of Mo=O and the stretching and bending vibrations of Mo–O–Mo, respectively [22]. These similar FT-IR results also indicate the maintenance of the $MoO_3$ crystal structure.

UV–Vis diffuse reflection spectroscopy was employed to study the impact of oxygen vacancies on the optical characteristics of $MoO_3$ (Fig. S6 in the ESM). The energy band gaps of the samples

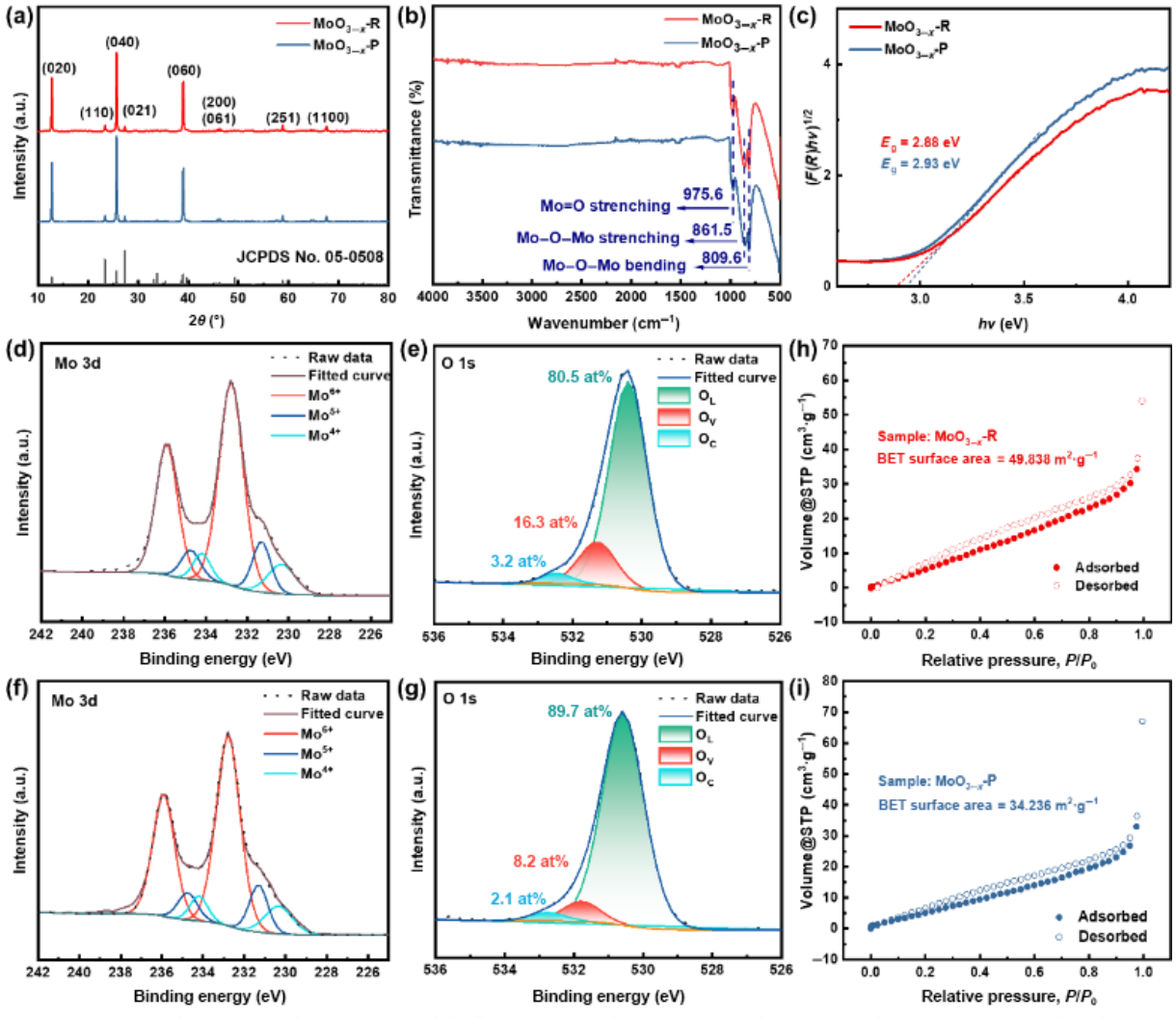


**Fig. 2** (a) PXRD patterns of $MoO_{3-x}$-R and $MoO_{3-x}$-P microbelts from 10° to 80°. (b) FT-IR spectra of $MoO_{3-x}$-R and $MoO_{3-x}$-P. (c) Tauc plots of $MoO_{3-x}$-R and $MoO_{3-x}$-P. Mo 3d and O 1s spectra of (d, e) $MoO_{3-x}$-R and (g, h) $MoO_{3-x}$-P. $N_2$ adsorption-desorption isotherms and BET-specific surface areas of (f) $MoO_{3-x}$-R and (i) $MoO_{3-x}$-P.

were estimated via the Kubelka-Munk formula [23]. As illustrated in Fig. 2(c), the bandgap values of $MoO_{3-x}$-R and $MoO_{3-x}$-P are 2.88 and 2.93 eV, which are attributed to the different $O_v$ concentrations.

XPS was employed to reveal the surface elemental composition and chemical state of $MoO_{3-x}$-R and $MoO_{3-x}$-P. As shown in Fig. S7 in the ESM, the full survey spectra reveal the core-level peaks of Mo 3d and O 1s. As depicted in Fig. 2(d), the peaks at 232.8 and 235.9 eV in the Mo 3d spectra are attributed to $Mo^{6+}$, the two peaks located at 231.3 and 234.8 eV are associated with $Mo^{5+}$, and the additional peaks at 234.2 and 230.3 eV are ascribed to $Mo^{4+}$. Importantly, the presence of these three similar peak sets can also be observed in $MoO_{3-x}$-P (Fig. 2(f)), indicating the coexistence of $Mo^{6+}$, $Mo^{5+}$, and $Mo^{4+}$ in both samples. Furthermore, the atomic percentages of different Mo species over $MoO_{3-x}$ were calculated. As shown in Table S1 in the ESM, both $MoO_{3-x}$ powders show that the surface Mo species were primarily in the form of $Mo^{6+}$ (70.5 % and 73.8%, respectively). Notably, $MoO_{3-x}$-R has a higher content (29.5%) of $Mo^{5+}$ and $Mo^{4+}$, whereas that of $MoO_{3-x}$-P is 26.2%. The generation of Mo with low valence is related to the occurrence of oxygen vacancies [24]. As shown in Fig. 2(e), the O 1s spectra of $MoO_{3-x}$-R display three peaks at approximately 530.4, 531.3, and 532.5 eV, representing lattice oxygen ($O_{latt}$), $O_V$, and chemisorbed oxygen species ($O_C$), respectively. Similar peaks at 530.5, 531.8, and 532.8 eV can also be found in the O 1s spectra of $MoO_{3-x}$-P (Fig. 3(g)).

The Brunauer–Emmet–Teller (BET)-specific surface areas and Barrett–Joyner–Halenda (BJH) pore distributions were determined for the $MoO_{3-x}$-R and $MoO_{3-x}$-P microbelts. The isotherm plots of $MoO_{3-x}$-R and $MoO_{3-x}$-P are depicted in Figs. 2(h) and 2(i). The calculated BET-specific surface areas of $MoO_{3-x}$-R and $MoO_{3-x}$-P are 49.84 and 34.24 $m^2 \cdot g^{-1}$, respectively. Figure S8 and Table S2 in the ESM show that the average pore sizes of $MoO_{3-x}$-R and $MoO_{3-x}$-P are 3.50 and 2.97 nm, respectively. Moreover, $MoO_{3-x}$-R has a greater total pore volume of 0.104 $cm^3 \cdot g^{-1}$, whereas that of $MoO_{3-x}$-P is 0.083 $cm^3 \cdot g^{-1}$. The modified surface characteristics of $MoO_{3-x}$-R enhance the adsorption and diffusion of gas molecules, thus attaining superior sensing capacity [25].

### 3.2 Gas-sensing performance

A schematic diagram of the gas sensor is displayed in Fig. 3(a). Bulk $MoO_3$, $MoO_{3-x}$-R, and $MoO_{3-x}$-P microbelts were measured at ambient temperature (22±1 °C). The effect of the sensing layer thickness was first investigated (Fig. S9 in the ESM), indicating that the 1-layer sensor has the highest response value. Figure S10 in the ESM shows the resistance changes of the gas sensors in

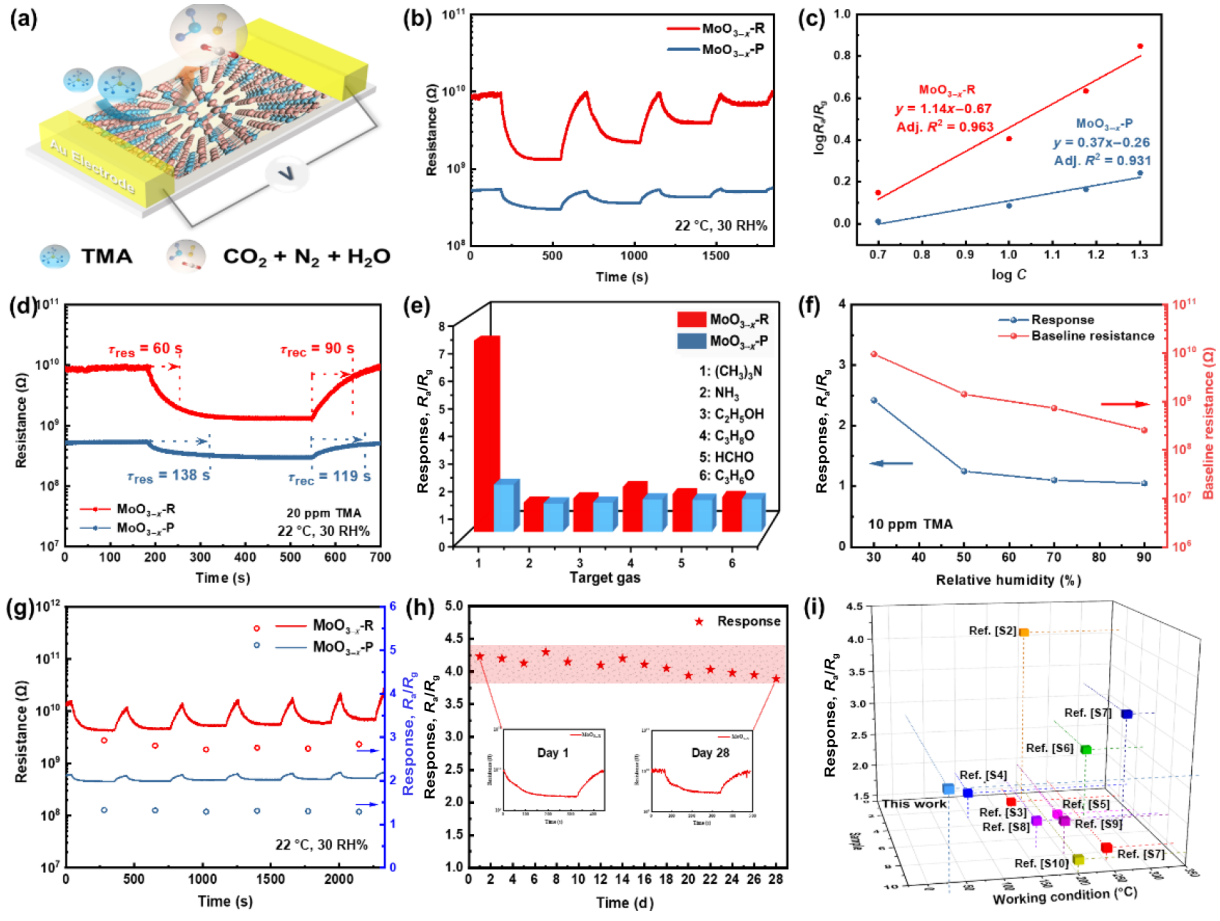


**Fig. 3** (a) Schematic diagram of oxygen vacancy-mediated $MoO_3$ microbelt-based gas sensor. (b) Dynamic resistance curves of $MoO_{3-x}$-R and $MoO_{3-x}$-P to 5–20 ppm TMA at 22 °C and 30 RH%. (c) Linear relationship between the log*S* and log*C* of all sensors. (d) Responses/recovery times of $MoO_{3-x}$-R and $MoO_{3-x}$-P to 20 ppm TMA. (e) Selectivity to 20 ppm TMA and other interfering gases of pristine $MoO_{3-x}$-R and $MoO_{3-x}$-P. (f) Variations in baseline resistance and response values of $MoO_{3-x}$-R and $MoO_{3-x}$-P vs. relative humidity. (g) Recyclability of $MoO_{3-x}$-R and $MoO_{3-x}$-P sensors to 10 ppm TMA after 6 cycles. (h) Stable response of $MoO_{3-x}$-R sensor to 15 ppm TMA over 28 d. (i) Comparison of TMA sensitivity between this work and recently reported metal oxide-based gas sensors.

response to 20 ppm TMA. Notably, the resistance of bulk $MoO_3$ hardly varies from that of TMA, whereas that of the $MoO_{3-x}$-R and $MoO_{3-x}$-P microbelts significantly changes. Figure 3(b) and Fig. S11 in the ESM show the transient response/recovery curves and response values of $MoO_{3-x}$-R and $MoO_{3-x}$-P to 5–20 ppm TMA. $MoO_{3-x}$-R shows the highest response values of 1.41–7.09 for 5–20 ppm TMA, whereas those of $MoO_{3-x}$-P range from 1.03 to 1.75.

As shown in Fig. 3(c), $MoO_{3-x}$-R presents a good linear response ($R^2$ = 0.963) and the highest sensitivity of 1.14 $ppm^{-1}$, whereas the sensitivity of $MoO_{3-x}$ decreases to 0.37 $ppm^{-1}$. To obtain the theoretical LOD = $3RMS_{noise}$/slope [26], the noise of the $MoO_{3-x}$-R and $MoO_{3-x}$-P sensors ($RMS_{noise}$) was first calculated as 0.144 and 0.601, respectively. The corresponding LODs are approximately 0.4 and 4.8 ppm, respectively. As shown in Fig. 3(d), the $MoO_{3-x}$-R gas sensor exhibited a quicker response/recovery speed to 20 ppm TMA (60 s/90 s) than did the $MoO_{3-x}$-P sensor, which had response/recovery times of 138 and 119 s, respectively. The enhanced mechanisms of the LOD and response/recovery speed will be discussed later.

Selectivity is a crucial parameter in practical applications. $MoO_{3-x}$-R and $MoO_{3-x}$-P microbelt gas sensors were used to detect $C_3H_9N$, $NH_3$, $C_3H_8O$, $C_2H_5OH$, HCHO, and $C_3H_6O$ at 20 ppm. As shown in Fig. 3(e) and Fig. S12 in the ESM, $MoO_{3-x}$-R exhibited a notably greater response of 7.1 to TMA, while the responses to $NH_3$, $C_3H_8O$, $C_2H_5OH$, HCHO, and $C_3H_6O$ were 1.08, 1.23, 1.66, 1.39, and 1.28, respectively. However, $MoO_{3-x}$-P shows a similar response to all the target gases, revealing the remarkable selectivity of the $MoO_{3-x}$-R microbelts toward TMA.

Alterations in relative humidity levels may impact gas sensors operating at room temperature. Therefore, the as-fabricated $MoO_{3-x}$-R sensor was evaluated at RH values ranging from 30% to 90% (Fig. S13 in the ESM). In Fig. 3(f), the response values to 10 ppm TMA are 2.42, 1.27, 1.18, and 1.15, respectively. Moreover, the baseline resistance of the $MoO_{3-x}$-R-based sensor also decreased with increasing relative humidity. This phenomenon can be ascribed to the electron–donating behavior of water molecules [27]. Consequently, the presence of water vapor molecules leads to a reduction in the baseline resistance [28]. Additionally, the water molecules adsorbed on the surface take up the active sites of the $MoO_{3-x}$-R sensor, preventing TMA from interacting with the oxygen species present, thus leading to a decrease in the resistance of the sensor caused by TMA [29]. When the relative humidity becomes high (50%–90%), the adsorbed water molecules gradually reach saturation, thus resulting in a slight drop in the response values [17].

The operational stability of the $MoO_{3-x}$-R sensor was also investigated. Figure 3(g) shows the reproducible sensing behavior of $MoO_{3-x}$-R toward 10 ppm TMA across six cycles, with stable response values averaging approximately 2.8, whereas that of $MoO_{3-x}$-R is 1.3. Figure 3(h) shows the stable response of $MoO_{3-x}$-R toward 15 ppm TMA over 28 days, indicating that the as-

fabricated gas sensor has excellent operational stability. In addition, Fig. 3(i) and Table S3 in the ESM compare the TMA sensing properties of $MoO_{3-x}$-R with those of other metal oxide-based gas sensors recently reported in the literature. $MoO_{3-x}$-R microbelts exhibit significantly lower working temperatures, higher sensitivities, and better LODs.

### 3.3 Gas-sensing mechanisms

The gas-sensing mechanisms are often elucidated by the chemical redox reactions that take place between adsorbed oxygen anions and target gas molecules [30,31]. As shown in Fig. 4(a) and Table S4 in the ESM, when the sensing layers meet air at room temperature, the adsorbed oxygen species on the surface capture electrons from the conduction band to form charged oxygen species ($O_2^-$). Then, the TMA molecules react with $O_2^-$ and release the electrons back to the conduction bands, resulting in a decrease in resistance.

The enhanced TMA sensing mechanisms of the $MoO_{3-x}$-R microbelts are elucidated from the aspects of nanostructure, specific surface area, and oxygen vacancies. First, $MoO_{3-x}$-R microbelts have relatively small diameters (Fig. 1(d)), which contributes to facilitating the maximum change in resistance of the sensing materials upon gas molecule adsorption [32]. Second, the $MoO_{3-x}$-R microbelts have a larger specific surface area, pore size, and total pore volume to offer more active sites and diffusion panels for adsorbed oxygen and TMA gas molecules (Figs. 2(f) and 2(i) and Table S2 in the ESM). Third, the higher peak intensity of $MoO_{3-x}$-R at 530 nm indicates a high concentration of oxygen vacancies (Fig. 4(b)) [33,34]. The enriched $O_V$s and $O_C$s (Fig. 2(g) and Table S5 in the ESM) improved the surface activity and gas adsorption, thus enhancing the reaction between the sensing layer and TMA [35]. The experimental results corroborate the suggested improvements in the sensing mechanisms. In Fig. 4(c), $MoO_{3-x}$-R presents a higher baseline resistance ($R_a$, $9.16\times10^9$ Ω) and a greater resistance ($\Delta R$, $7.85\times10^9$ Ω), whereas those of $MoO_{3-x}$-P are $5.40\times10^8$ and $2.39\times10^8$ Ω, respectively.

To better understand the enhanced sensing mechanism, the adsorption behaviors of gas molecules on B-$MoO_3$, $MoO_{3-x}$-R, and $MoO_{3-x}$-P were studied via DFT calculations. The optimal geometry structures were first obtained (Fig. S15 in the ESM). Then, the adsorption energies and electron density differences of the TMA gas molecules on B-$MoO_3$, $MoO_{3-x}$-R, and $MoO_{3-x}$-P were calculated. In Figs. 4(d)–4(i), for the $MoO_{3-x}$-R crystal

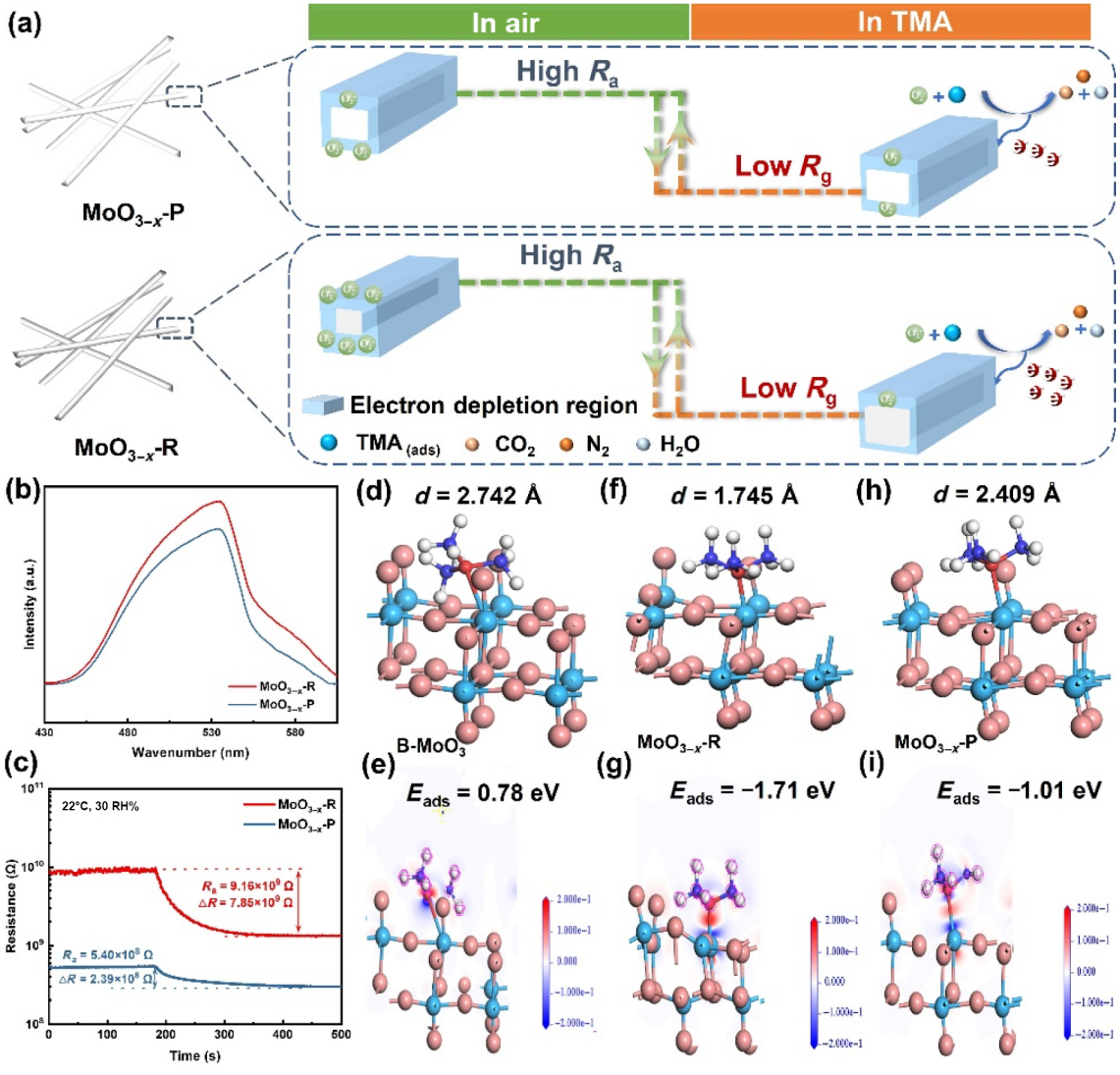


**Fig. 4** (a) Adsorption and reaction model of TMA sensing process on surface of $MoO_{3-x}$-R and $MoO_{3-x}$-P microbelts. (b) PL spectra of $MoO_{3-x}$-R and $MoO_{3-x}$-P. (c) Baseline resistance values and their variations for $MoO_{3-x}$-R and $MoO_{3-x}$-P in air and TMA. Geometric structure and electron density difference for TMA adsorption systems of (d, e) B-$MoO_3$, (f, g) $MoO_{3-x}$-R, and (h, i) $MoO_{3-x}$-P. Blue and red regions represent electron accumulation and depletion, respectively. Isosurface value is 0.1.

structure, the adsorption energy of TMA and the distance are −1.71 eV and 1.745 Å, which are much smaller than those of B-$MoO_3$ (0.78 eV, 2.742 Å) and $MoO_{3-x}$-P (−1.01 eV, 2.409 Å), indicating a stronger adsorption capacity for TMA on $MoO_{3-x}$-R [36,37]. Furthermore, the electron density difference across the TMA-adsorbed structural models reveals that a higher electron concentration accumulates in the interface region near $MoO_{3-x}$-R. These results verify that increasing the number of oxygen vacancies could further increase gas adsorption and expedite electron transfer, thereby contributing to improving the gas-sensing properties.

The electronic structure modulation of the $MoO_{3-x}$-R and $MoO_{3-x}$-P microbelts also improved the sensing properties. The valence band positions and work functions of each sample were obtained via VB-XPS (Figs. 5(a) and 5(d)) and DFT simulations (Figs. 5(b) and 5(e)). The valence band position and work function of $MoO_{3-x}$-R are 3.17 and 5.90 eV, respectively, whereas those of $MoO_{3-x}$-P are 3.35 and 6.56 eV, respectively. Notably, the lower work function contributes to electron transfer and then enhances the room-temperature reaction activity. On the basis of the obtained band gap values in Fig. 2(c), the energy band diagram of each sample is shown in Fig. 5(c).

Figures 5(f) and 5(i) show the calculated density of states (DOS) of $MoO_{3-x}$-R and $MoO_{3-x}$-P. The rich oxygen vacancies introduce a new defect level [38], resulting in a narrower band gap in $MoO_{3-x}$-R. This result is consistent with the experimental analysis. Furthermore, by checking the d-band for $MoO_{3-x}$-R and $MoO_{3-x}$-P, Figs. 5(g) and 5(h) show a significant upshift in the d-band center ($\varepsilon_d$) from −6.993 to −6.771 eV. According to the d-band model, the upshift of $\varepsilon_d$ led to the emergence of a distinct antibonding state positioned beyond the Fermi level, which strengthened the interaction between TMA and $MoO_{3-x}$-R [39,40]. On the basis of the above results, the modulated electronic structure improved the room-temperature gas-sensing performance after the incorporation of many oxygen vacancies.

To gain deeper insights into the enhanced TMA sensing capabilities, MD simulations were conducted to explore the dynamic behavior of TMA diffusion on the B-$MoO_3$, $MoO_{3-x}$-R, and $MoO_{3-x}$-P samples (Figs. 6(a)–6(d) and Fig. S16 in the ESM). The mean square displacement (MSD) is computed to quantitatively reflect the interaction between the sensing layer and TMA [41]. Notably, B-$MoO_3$ has a much higher MSD value than the $MoO_{3-x}$-P and $MoO_{3-x}$-R samples do (Fig. 6(e)). Moreover, the corresponding diffusion coefficient of TMA over B-$MoO_3$ is greater than those of the $MoO_{3-x}$-P and $MoO_{3-x}$-R samples (Fig. 6(g)), indicating a stronger TMA affinity for oxygen-vacancy state-sensing material systems. Therefore, the increased accumulation of TMA molecules around $MoO_{3-x}$-R facilitates the chemisorption of TMA gas molecules on the sensing layer, enhancing the sensor response. Following the 10 ps simulation,

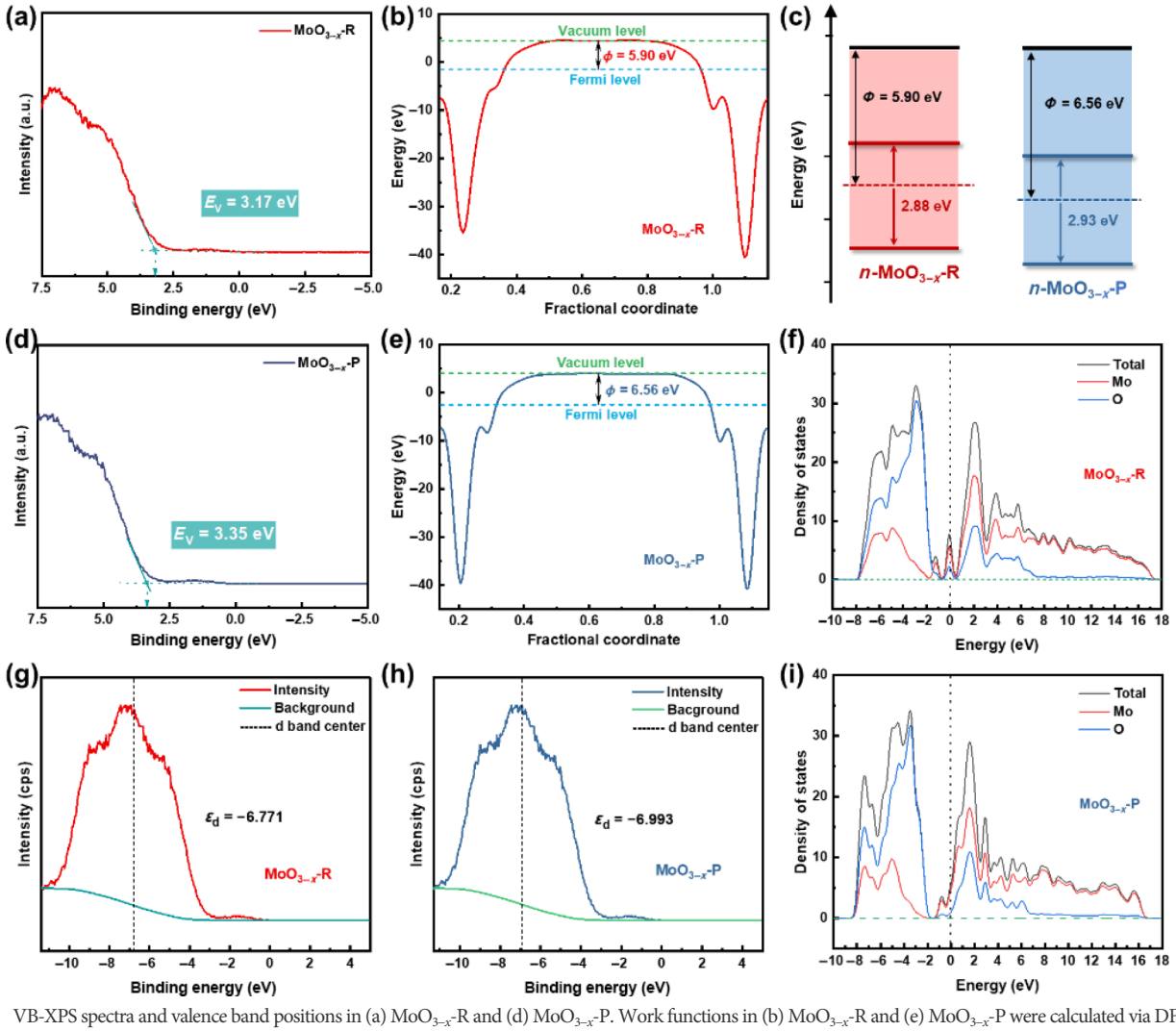


**Fig. 5** VB-XPS spectra and valence band positions in (a) $MoO_{3-x}$-R and (d) $MoO_{3-x}$-P. Work functions in (b) $MoO_{3-x}$-R and (e) $MoO_{3-x}$-P were calculated via DFT. (c) Band structure of $MoO_{3-x}$-R and $MoO_{3-x}$-P. d-band centers in (g) $MoO_{3-x}$-R and (h) $MoO_{3-x}$-P. PDOSs in (f) $MoO_{3-x}$-R and (i) $MoO_{3-x}$-P.

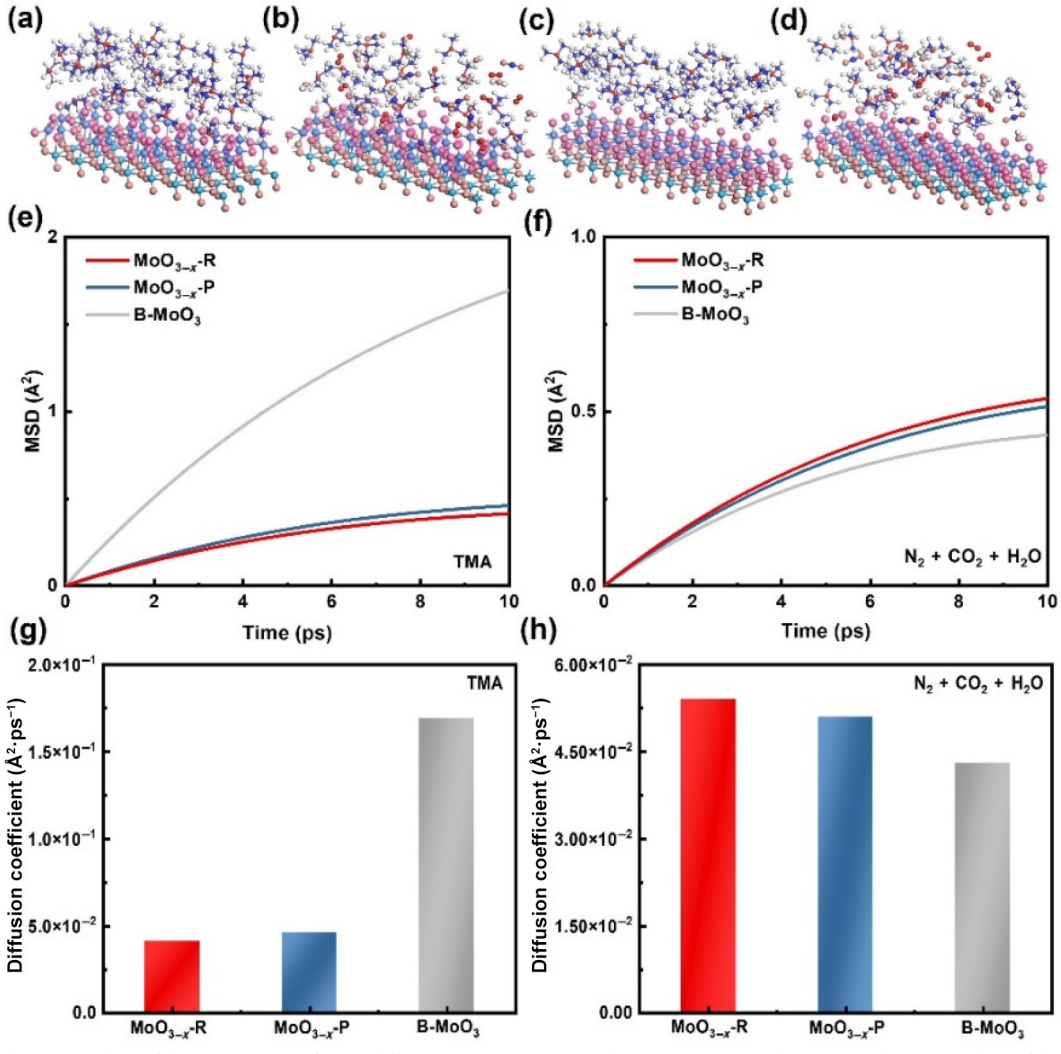


**Fig. 6** MD simulation snapshots of dynamic process of TMA diffusion on (a) $MoO_{3-x}$-R and (c) $MoO_{3-x}$-P samples. MD simulation snapshots of dynamic process of nitrogen, carbon dioxide, and water vapor diffusion in (b) $MoO_{3-x}$-R and (d) $MoO_{3-x}$-P samples. MSDs of (e) TMA and (f) nitrogen, carbon dioxide, and water vapor on $MoO_{3-x}$-R, $MoO_{3-x}$-P, and B-$MoO_3$ samples. Diffusion coefficients of (g) TMA and (h) nitrogen, carbon dioxide, and water vapor on $MoO_{3-x}$-R, $MoO_{3-x}$-P, and B-$MoO_3$.

the MSD curves and diffusion coefficient display weaker interactions between the total reaction products (nitrogen, carbon dioxide, and water vapor) and $MoO_{3-x}$-R than those of the other two samples (Figs. 6(f) and 6(h)), revealing easier desorption of the reaction products on $MoO_{3-x}$-R and shorter recovery time [42].

### 3.4 Applications in scenario

The as-fabricated $MoO_{3-x}$-R sensor was first employed to monitor TMA released from 20 g *Cod* fish through a homemade detection system (Fig. S17 in the ESM). As shown in Fig. S18 in the ESM, fish freshness was assessed by detecting TMA and measuring the pH values during storage at different times. Figure S21 in the ESM displays optical images of *Cod* fish stored for various periods and the corresponding electrical resistance variation of the $MoO_{3-x}$-R gas sensor. The fish shift toward darker hues and softer muscle tissue, indicating the start and progression of fish spoilage. As shown in Fig. S22 in the ESM, the pH decreased from 6.865 to 6.73 in the first 2 days, which was attributed to the production of lactic acid, adenosine triphosphate (ATP), and $H^+$ [43]. During the subsequent 6 days, the pH increased from 7.136 to 7.927, which correlated with the breakdown of proteins and the generation of alkaline metabolites [43,44]. As shown in Fig. 7(a), the response of the $MoO_{3-x}$-R gas sensor linearly increased from 1.26 to 11.73 as the storage time increased, indicating the quantitative and predictive ability of the $MoO_{3-x}$-R sensor.

With respect to the sensor responses, pH levels, and changes in the physical properties of the fish, principal component analysis (PCA) and linear discriminant analysis (LDA) were employed to categorize fish freshness. In Fig. 7(b) and Fig. S23 in the ESM, the total contribution rates from the principal components accounted for 93.1% and 99.5%, respectively. The fish remained fresh during the first 2 days (green oval), subsequently entered the early spoil stage by the 3rd and 4th days (brown oval), and were fully spoiled by the 5th and 8th days (pink oval). As shown in Fig. 7(c), the contribution rates of LDA1 and LDA2 were 67.2% and 32.8%, respectively, and the total contribution rates reached 100%. The results of this analysis coincide with the PCA results. The above results affirm the potential of the $MoO_{3-x}$-R gas sensor for rapid and nondestructive fish freshness detection.

For further practical purposes, a portable TMA sensing device composed of a $MoO_{3-x}$-R sensor, a circuit module for signal collection and data processing, and a Bluetooth transmission unit was developed (Fig. 7(d) and Fig. S24 in the ESM). The device is capable of continuously detecting and acquiring signals as well as processing data while operating at room temperature. These results can be displayed on a self-programmed mobile app,

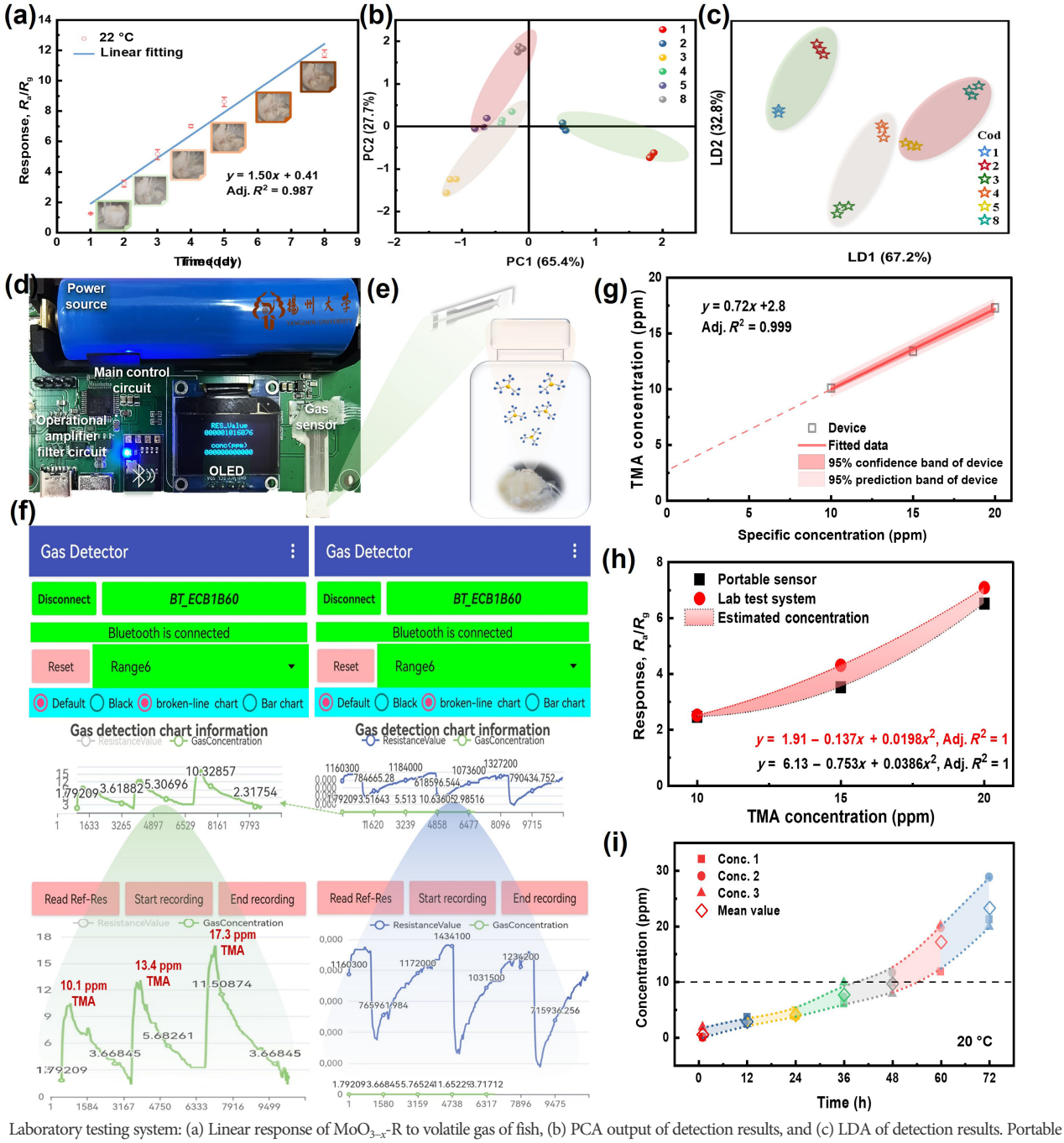


**Fig. 7** Laboratory testing system: (a) Linear response of $MoO_{3-x}$-R to volatile gas of fish, (b) PCA output of detection results, and (c) LDA of detection results. Portable sensor device: (d) optical photograph of portable device. (e) Schematic diagram of headspace sampling and detection. (f, h) Concentration calibration of $MoO_{3-x}$-R sensor in a laboratory environment. *X*-axis represents time (signal acquisition interval of 50 ms), and *Y*-axis represents resistance (kΩ). (i) On-field detection of *Cod* fish (30 g) stored at 20 °C for 72 h.

enabling wireless and real-time monitoring. We employed this device to detect and identify *Cod* fish at different freshness stages for demonstration (Fig. 7(e)). Before the on-field operation, sensor calibration was demonstrated, where the injected TMA concentration was precisely controlled. The portable sensor device displays an exceptional response/recovery curve, and the corresponding TMA concentration is 10.1 ppm (Fig. S25 in the ESM). Furthermore, TMAs of 15 and 20 ppm are also used for calibration, as shown in Figs. 7(f) and 7(g). The portable sensor shows reversible resistance curves and a linear response, while the corresponding TMA concentrations are 13.4 and 17.3 ppm, respectively. Hence, portable sensors tend to overvalue the injected gas concentration. In this case, the lower measured response values may have been caused by the incompletely sealed and isolated homemade 3D-printed enclosure (Fig. S26 in the ESM). Therefore, the portable sensor device was calibrated to identify such an overestimation.

As displayed in Fig. 7(h), the real detection result is expected to fall in the red area between the two calibration lines. The portable sensor system was then used for on-field detection of volatile TMA released from *Cod* fish. The volatile TMA was produced through the headspace sampling method, and the relative humidity of the environment and released gas was controlled at 65–72 RH% to ensure a negligible effect of humidity change (Fig.

S27 in the ESM). As shown in Fig. S28 in the ESM, the portable device displays distinct time-dependent resistance curves toward the fish samples during different storage periods and freshness stages as the TMA concentration increases and the freshness changes at 20 °C. As depicted in Fig. 7(i), the real TMA concentrations were lower than 10 ppm at 36 h but rapidly increased after 48 h, indicating the occurrence of fish spoilage. These results confirm the broad application prospects of portable room-temperature gas sensor devices.

## 4 Conclusions

In summary, a novel room-temperature operational gas sensor device based on one-dimensional $MoO_3$ microbelts with controlled oxygen vacancies was successfully designed and demonstrated. Comprehensive characterization and structural analysis confirmed the formation of $MoO_{3-x}$-R and $MoO_{3-x}$-P microbelts. The experimental results revealed that $MoO_{3-x}$-R exhibited an enhanced response to 5–20 ppm TMA, satisfactory selectivity, a low limit of detection of 400 ppb, and good repeatability. Modifications in the nanostructure, specific surface area, oxygen vacancies, and electronic structure improved the redox kinetics and excellent sensing performance. The combination of DFT and MD simulations provides valuable insights into the high sensitivity and rapid response/recovery of the $MoO_{3-x}$-R-based sensor. In addition, the developed portable device for on-field monitoring also demonstrated precise quantification of the released TMA concentration and reliable nondestructive assessment of fish freshness. This work presents a universal design principle of oxygen vacancy-engineered interfacial charge transfer kinetics in metal oxides, enabling the development of gas sensor devices for broad applications.

### Acknowledgements

This work is supported by the National Natural Science Foundation of China (No. 52402202), the Natural Science Youth Foundation of Jiangsu Province of China (No. BK20240933), the Outstanding Youth Foundation of Jiangsu Province of China (No. BK20211548), the Yangzhou Science and Technology Plan Project (No. YZ2023246), and Qinglan Project of Yangzhou University.

### Author contributions

Kaidi Wu: Conceptualization, methodology, investigation, funding acquisition, writing—original draft, review, and editing. Zhijie Xu: Methodology and investigation. Kaichun Xu: Investigation. Jinyong Xu: Investigation, writing—review & editing. Yifan Luo: Writing—review & editing. Marc Debliquy: Supervision, writing—review & editing. Chao Zhang: Conceptualization, supervision, resources, writing—review & editing.

### Availability of data and materials

The data that support the findings of this study are available from the corresponding author upon reasonable request.

### Competing interests

The authors have no competing interests to declare that are relevant to the content of this article. The author Chao Zhang is the Editorial Committee member of this journal.

### Electronic Supplementary Material

Supplementary material is available in the online version of this article at https://doi.org/10.26599/JAC.2025.9221102.

## References

[1] Jian YY, Hu WW, Zhao ZH, *et al.* Gas sensors based on chemi-resistive hybrid functional nanomaterials. *Nano-Micro Lett* 2020, **12**: 71.

[2] Nguyen LHT, Navale ST, Yang DH, *et al.* Fe-based metal–organic framework as a chemiresistive sensor for low-temperature monitoring of acetone gas. *Sensor Actuat B Chem* 2023, **388**: 133799.

[3] He XX, Chai HF, Luo YF, *et al.* Metal oxide semiconductor gas sensing materials for early lung cancer diagnosis. *J Adv Ceram* 2023, **12**: 207–227.

[4] Sharma A, Eadi SB, Noothalapati H, *et al.* Porous materials as effective chemiresistive gas sensors. *Chem Soc Rev* 2024, **53**: 2530–2577.

[5] Sun YH, Zhang DZ, Tang MC, *et al.* Trimethylamine gas sensor based on bimetallic Ag/Cu@$CuFe_2O_4$: Experiment and DFT calculation. *J Alloys Compd* 2025, **1010**: 177662.

[6] Wang D, Zhang D, Yang Y, *et al.* Multifunctional latex/polytetrafluoroethylene-based triboelectric nanogenerator for self-powered organ-like MXene/metal–organic framework-derived CuO nanohybrid ammonia sensor. *ACS Nano* 2021, **15**: 2911–2919.

[7] Hassan M, Liu SW, Liang ZP, *et al.* Revisiting traditional and modern trends in versatile 2D nanomaterials: Synthetic strategies, structural stability, and gas-sensing fundamentals. *J Adv Ceram* 2023, **12**: 2149–2246.

[8] Sui XX, Zhang DZ, Wang JH, *et al.* Ppb-level detection of trimethylamine as biomarker in exhaled gas based on $MoO_3/V_2O_5$ hierarchical heterostructure. *J Alloys Compd* 2023, **968**: 172104.

[9] Wu ZX, Zhao Y, Jin W, *et al.* Recent progress of vacancy engineering for electrochemical energy conversion related applications. *Adv Funct Mater* 2021, **31**: 2009070.

[10] Zhang H, Zhang DZ, Yang Y, *et al.* Eco-friendly triboelectric nanogenerator for self-powering stacked $In_2O_3$ nanosheets/PPy nanoparticles-based $NO_2$ gas sensor. *Nano Energy* 2024, **128**: 109978.

[11] Aysha Parveen R, Vinoth E, Harish S, *et al.* Oxygen vacancies mediated α-$MoO_3$ nano-ribbons by Cu doping for highly sensitive, selective and rapid detection of hazardous $NO_2$ for gas sensor application. *Sensor Actuat B Chem* 2023, **389**: 133810.

[12] Zhou YW, Luo YF, Zheng ZC, *et al.* Urchin-like Na-doped zinc oxide nanoneedles for low-concentration and exclusive VOC detections. *J Adv Ceram* 2024, **13**: 507–517.

[13] Zeb S, Yang Z, Hu RM, *et al.* Electronic structure and oxygen vacancy tuning of Co & Ni co-doped $W_{18}O_{49}$ nanourchins for efficient TEA gas sensing. *Chem Eng J* 2023, **465**: 142815.

[14] Phyo S, Kim S, Lee H, *et al.* Adsorption enhancement of hazardous odor gas using controlled thermal oxidation of activated carbon. *J Clean Prod* 2023, **393**: 136261.

[15] Chen SH, Duan XY, Liu C, *et al.* La–Ce-MOF nanocomposite coated quartz crystal microbalance gas sensor for the detection of amine gases and formaldehyde. *J Hazard Mater* 2024, **467**: 133672.

[16] Berhe Gebreegziabher T, Wang S, Nam H. Adsorption of $H_2S$, $NH_3$ and TMA from indoor air using porous corncob activated carbon: Isotherm and kinetics study. *J Environ Chem Eng* 2019, **7**: 103234.

[17] Wu KD, He XX, Ly A, *et al.* Highly sensitive and selective gas sensors based on 2D/3D $Bi_2MoO_6$ micro-nano composites for trimethylamine biomarker detection. *Appl Surf Sci* 2023, **629**: 157443.

[18] Wu KD, Xu JY, Debliquy M, *et al.* Synthesis and $NH_3$/TMA sensing properties of $CuFe_2O_4$ hollow microspheres at low working temperature. *Rare Metals* 2021, **40**: 1768–1777.

[19] Zhao G, Sun J, Zhang M, *et al.* Highly strain-stable intrinsically stretchable olfactory sensors for imperceptible health monitoring. *Adv Sci* 2023, **10**: 2302974.

[20] Chen Q, Zheng JF, Liu XQ, *et al.* First-principles investigations on the mechanism of highly sensitive and selective trimethylamine sensing in $MoO_3$. *Appl Surf Sci* 2020, **524**: 146520.

[21] Wang P, Guo S, Hu Z, *et al.* Single-atom Cu stabilized on ultrathin $WO_{2.72}$ nanowire for highly selective and ultrasensitive ppb-level toluene detection. *Adv Sci* 2023, **10**: 2302778.

[22] Sen SK, Munshi MR, Kumar A, *et al.* Structural, optical, magnetic, and enhanced antibacterial properties of hydrothermally synthesized Sm-incor22porating α-$MoO_3$ 2D-layered nanoplates. *RSC Adv* 2022, **12**: 34584–34600.

[23] Cui SX, Wu HP, Hu ZG, *et al.* The antiperovskite-type oxychalcogenides $Ae_3Q$ [$GeOQ_3$] (Ae = Ba, Sr; Q = S, Se) with large second harmonic generation responses and wide band gaps. *Adv Sci* 2023, **10**: 2204755.

[24] Xie WW, Huang JH, Huang LT, *et al.* Novel fluorine-doped cobalt molybdate nanosheets with enriched oxygen-vacancies for improved oxygen evolution reaction activity. *Appl Catal B Environ* 2022, **303**: 120871.

[25] Wu KD, Chai HF, Xu KC, *et al.* Effect of {010}crystal facets of $Bi_2MoO_6$ and 1D/2D heterostructures for conductometric room temperature $NH_3$ gas sensors. *Sensor Actuat B Chem* 2023, **376**: 132983.

[26] Wu KD, Debliquy M, Zhang C. Room temperature gas sensors based on Ce doped $TiO_2$ nanocrystals for highly sensitive $NH_3$ detection. *Chem Eng J* 2022, **444**: 136449.

[27] Şahin Z, Meunier-Prest R, Dumoulin F, *et al.* Tuning of organic heterojunction conductivity by the substituents' electronic effects in phthalocyanines for ambipolar gas sensors. *Sensor Actuat B Chem* 2021, **332**: 129505.

[28] Liu Y, Li XH, Li XW, *et al.* Highly permeable $WO_3$/$CuWO_4$ heterostructure with 3D hierarchical porous structure for high-sensitive room-temperature visible-light driven gas sensor. *Sensor Actuat B Chem* 2022, **365**: 131926.

[29] Guo WW, Shuai YT, Liu XC, *et al.* A n-butanol gas sensor with enhanced gas sensing performance based on co-doped $BiVO_4$ polyhedrons. *Sensor Actuat B Chem* 2022, **354**: 131221.

[30] Ji HC, Zeng W, Li YQ. Gas sensing mechanisms of metal oxide semiconductors: A focus review. *Nanoscale* 2019, **11**: 22664–22684.

[31] Wu KD, Zhang WT, Zheng ZC, *et al.* Room-temperature gas sensors based on titanium dioxide quantum dots for highly sensitive and selective $H_2S$ detection. *Appl Surf Sci* 2022, **585**: 152744.

[32] Yang BX, Myung NV, Tran TT. 1D metal oxide semiconductor materials for chemiresistive gas sensors: A review. *Adv Electron Mater* 2021, **7**: 2100271.

[33] Ri JS, Li XW, Shao CL, *et al.* Sn-doping induced oxygen vacancies on the surface of the $In_2O_3$ nanofibers and their promoting effect on sensitive $NO_2$ detection at low temperature. *Sens Actuat B Chem* 2020, **317**: 128194.

[34] Li X, Yang HM, Wu QR, *et al.* Molecular traps and exposed Mo sites induced by oxygen knockout enhanced $H_2S$ sensing of $MoO_3$ nanoflowers. *Appl Surf Sci* 2023, **612**: 155845.

[35] Zhao L, Yu CC, Xin CC, *et al.* Increasing the catalytic activity of $Co_3O_4$ via boron doping and chemical reduction for enhanced acetone detection. *Adv Funct Mater* 2024, **34**: 2314174.

[36] Zong B, Xu Q, Mao S. Single-atom Pt-functionalized $Ti_3C_2T_x$ field-effect transistor for volatile organic compound gas detection. *ACS Sens* 2022, **7**: 1874–1882.

[37] Zhang C, Han M, Xu K, *et al.* Advances in the application of density functional theory to the design of two-dimensional gas-sensitive materials. *Journal of Yangzhou University (Natural Science Edition)* 2025, **28**: 1–16, 34. (in Chinese)

[38] Wang ZL, Lin RJ, Huo YN, *et al.* Formation, detection, and function of oxygen vacancy in metal oxides for solar energy conversion. *Adv Funct Mater* 2022, **32**: 2109503.

[39] Wang Y, Fan G, Wang S, *et al.* Implanting $CoO_x$ clusters on ordered macroporous ZnO nanoreactors for efficient $CO_2$ photoreduction. *Adv Mater* 2022, **34**: 2204865.

[40] Ma ZF, Liu X, Wang XS, *et al.* Manipulating the d-band center enhances photoreduction of $CO_2$ to CO in $Zn_2GeO_4$ nanorods. *Chem Eng J* 2023, **468**: 143569.

[41] Kim DH, Chong S, Park C, *et al.* Oxide/ZIF-8 hybrid nanofiber yarns: Heightened surface activity for exceptional chemiresistive sensing. *Adv Mater* 2022, **34**: 2105869.

[42] Chu K, Luo YJ, Shen P, *et al.* Unveiling the synergy of O-vacancy and heterostructure over $MoO_{3-x}$/MXene for $N_2$ electroreduction to $NH_3$. *Adv Energy Mater* 2022, **12**: 2103022.

[43] Fang SL, Guan ZH, Su C, *et al.* Accurate fish-freshness prediction label based on red cabbage anthocyanins. *Food Control* 2022, **138**: 109018.

[44] Wu K, Debliquy M, Zhang C. Metal-oxide-semiconductor resistive gas sensors for fish freshness detection. *Compr Rev Food Sci F* 2023, **22**: 913–945.